Second-harmonic generation provides insight into the screening response of the liquid water interface

Kamal K. Ray[¥1], Aditya Limaye[¥2], Ka Chon Ng[1], Ankur Saha[1], Sucheol Shin[3], Biswajit Biswas[1], Marie-Pierre Gaigeot[4], Simone Pezzotti[5], Adam P. Willard*[2], and Heather C. Allen*[1]

[1] The Ohio State University, Department of Chemistry and Biochemistry, Columbus, OH 43210.

[2] MIT, Department of Chemistry, Cambridge, MA 02139.

[3]University of Texas at Austin, Department of Chemistry, Austin, TX 78712.

[4]Université Paris-Saclay, Univ Evry, CNRS, LAMBE UMR8587, 91025 Evry-Courcouronnes, France

[5]Ruhr University Bochum, Department of Physical Chemistry II, D-44801 Bochum, Germany

*allen@chemistry.ohio-state.edu

*awillard@mit.edu

We use second harmonic generation (SHG), molecular dynamics simulation, and theoretical modeling to study the response of the neat liquid water-air interface to changes in the potential of an external electrode positioned near the liquid, but out of direct contact. We observe a parabolic dependence of second harmonic intensity on applied potential. Based on standard theory, we associate this dependence with the response of the diffuse layer water molecules to changes in interfacial potential profile. Taking the literature value for this response leads to the unexpected conclusion that the electric fields within the diffuse layer are opposite in sign from those originating from the electrodes. This conclusion implies that the traditional continuum-based models of interfacial screening lack the complexity necessary to properly describe the potential profile of the liquid water-vapor interface. Effects such as overscreening in the topmost interfacial layer and extended correlations in the interfacial hydrogen bonding network may play a role in governing the response of the water interface to external fields.

1. Introduction

The physical, chemical, and biological properties of the liquid water-air interface are connected to, yet distinct from, those of the bulk liquid. These connections and distinctions must be characterized before we can fully understand the wide range of fundamental processes that are known to occur preferentially, or even exclusively, at the liquid water-air interface. In its most prevalent role - that of a solvent - water's

properties are determined by the nanoscale structure and dynamics of the molecular hydrogen bonding network.[1-4] At an interface, this network is strained and distorted, leading to anisotropy in the orientational distributions of water molecules as well as the electrostatic and dielectric properties that these distributions determine.[5-10] Resolving the details of these interfacial properties and how they respond to external fields is important because they influence interfacial solvation and transport (especially for charged species) as well as the thermodynamics and kinetics of aqueous interfacial chemical reactions, such as in assembly of supramolecular structures and in the regulation of the composition of our oceans and atmosphere.[11-18]

Over the last several decades, numerous scientific studies have been aimed at characterizing the molecular structure and associated electrostatic properties of the liquid water interface.[19-23] Despite these efforts, much remains to be understood about how the solvent properties of liquid water surfaces differ from those of the bulk and how those differences relate to water's interfacial molecular structure.[24-28] Water surface properties are difficult to measure because common experimental probes cannot isolate the signal of the interface from that of the bulk, and those that can offer low signal to noise and/or report indirectly on the microscopic details of the surface. Furthermore, the interpretation of interface-sensitive experiments is complicated by uncertainty in experimental probe-depth and limited reliability of theoretical models for treating interfacial systems.[29-30] Most notably, the various empirical force fields that are routinely used in molecular dynamics (MD) simulation (which are parameterized to reproduce bulk properties) differ in their predictions of many key features of water's interfacial molecular structure.[31-38]

The molecular structure of the liquid water interface can be studied by measuring its polarization response under an applied electric field.[31, 39-43] Electric fields interact with the dipole moments of water molecules, biasing their orientational alignment. Second harmonic generation (SHG) is sensitive to the net interfacial dipole,[44-48] and can thus report upon the average molecular alignment of the water surface, the diffuse layer, and how these layers change under external fields. SHG has also been used to report hyperpolarizabilities of bulk materials via electric field induced second harmonic (EFISH). In work presented here, although different to an EFISH measurement, the electric field is applied and dropped across both the air and the water phases as well as across the phase boundary, i.e. the liquid water - vapor interface; the SHG response then provides insight into organization of interfacial water and its inherent concentrations of hydroxyl and hydronium ions with and without an external field present. By further analyzing the SHG changes and, moreover, evaluating the data in the context of standard theories, we gain information about the configurational statistics of interfacial water molecules and thereby infer details of interfacial molecular structure that are not apparent via unbiased measurement alone.

Here we present SHG measurement of the air-water interface under an applied external potential. To analyze and interpret the results of these experiments, we use a combination of theoretical modeling and

molecular dynamics simulation. Specifically, we interpret the potential dependence of the second-harmonic intensity with a standard theory of interfacial second-harmonic response.[45, 49-50] In this theory, the net second-harmonic intensity is decomposed into separate contributions from the topmost interfacial layer (TIL), which exhibits significant broken symmetry (*e.g.*, dangling OH bonds), and the diffuse layer (DL), which is beyond the plane of the interface. After presenting the analysis and interpretation of our results, we conclude with a discussion of the shortcomings of present-day models and future needs.

2. Dependence of SHG intensity on externally applied electric field

We utilize SHG (SI, Fig. S1a) to probe the response of the water-air interface to a tunable externally applied electric field, building upon the work of Schmid, Hurd, and Snavely.[31, 39] The electric field is controlled by varying the potential of an electrode positioned in the air above a sample of neat liquid water; a second grounded electrode is directly below in the liquid (Fig. 1A). The experimental results, plotted in Fig. 1B, reveal the response in SHG intensity, using a *PP*, *SP and 45S* polarization combinations to then report $(\chi^{(2)}_{\text{eff, pp}})^2$ from negative to positive external potential (SHG polarization data and control experiments including NaCl electrolyte and variant air gap SHG experiments are shown in Figs. S2-S5). The observed SHG intensity is approximately parabolic (SI Fig. S1b), with a minimum at a positive potential of approximately +2.8 kV.

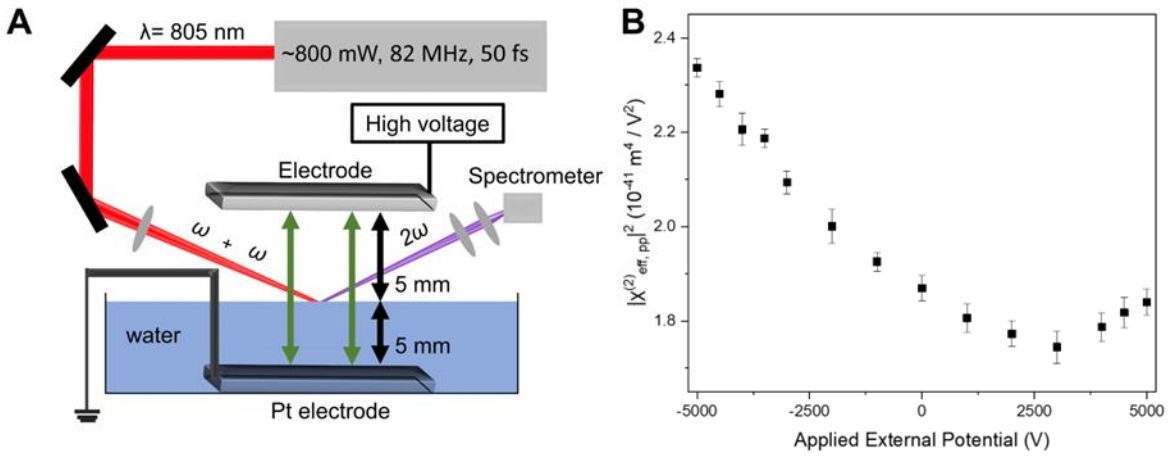

Figure 1. *Probing the response of the water – air interface to an applied external potential. (A) Schematic diagram of the high voltage second harmonic generation set-up at the sample. The pulsed laser (Ti:sapphire, λ= 805 ± 10 nm, repetition rate 82 MHz, <50 fs, polarized output, 10^{10} W/cm^2 power density) generates the second order intensity that is detected (180 second accumulated acquisitions). The high voltage set up is comprised of an air-phase electrode (DC-powered steel plate; 25 mm x 20 mm) and a grounded electrode in the condensed-phase (grounded parallel platinum plate; 25 mm x 22 mm). (B)*

Experimental second harmonic generation expressed as $(\chi^{(2)}_{\text{eff, pp}})^2$ *with the externally applied electric potential of -5 kV to +5 kV revealing an intensity minimum at applied bias of approximately +2.8 kV.*

We base our interpretation of the experimental results on a well-established theory of interfacial second order optical response.[30, 38, 49-53] In this theory the air-water interface is divided into three distinct regions: a topmost interfacial layer (TIL) of water molecules at the liquid surface (analogous to the binding interfacial layer (BIL) at solid-liquid interfaces[30, 53]), a diffuse layer (DL) with a width determined by the screening length of the solution, and a bulk region. The TIL contains the first monolayer of water molecules in highly anisotropic orientations due to the termination of the bulk hydrogen bonding network,[54-55] and thus includes the well-studied population of *dangling OH* molecules.[6, 37] The high level of anisotropy in the TIL leads to a significant SHG response.

By contrast, water molecules within the DL are subject to a more homogeneous and bulk-like molecular environment. However, this environment also includes a distribution of excess charge from ions (e.g., hydroxide and hydronium) driven to the interface by the applied external potential. The resulting electric fields, even if small in magnitude, contribute to symmetry breaking that generates SHG response. The width of the DL depends on the concentration of ions in solution but can be larger than that of the TIL by orders of magnitude at low ionic concentration. Together, the TIL and DL fully screen the external applied potential, leaving the bulk region purely isotropic and free of any static electric fields. The bulk is thus assumed to be SHG inactive.

The overall SHG signal, is given by the sum of TIL and DL contributions,[30, 52] yielding the following expression for SHG intensity:

$$\left(\chi^{(2)}_{\text{eff}}\right)^2 = \left(\chi^{(2)}_{\text{TIL}} + \chi^{(2)}_{\text{DL}}\right)^2 + C \tag{1}$$

where $\chi^{(2)}_{\text{TIL}}$ denotes the second-order susceptibility of the TIL, $\chi^{(2)}_{\text{DL}}$ is the second-order susceptibility of the diffuse layer that separates the TIL from the bulk liquid, and the quantity C denotes a field-independent background signal that arises in this experimental setup. In our analysis, C is given by the minimum value of $\left(\chi^{(2)}_{\text{eff}}\right)^2$. The DL contribution can be expressed as an integral over the DL region as,

$$\chi^{(2)}_{DL} = \int_{DL} E(z)\left[\chi^{(3)}_{\text{nuc}} + \chi^{(3)}_{\text{elec}}\right] e^{i\Delta k_z z} dz \equiv \chi^{(3)}_{\text{bulk}} \int_{DL} E(z) e^{i\Delta k_z z} dz \tag{2}$$

where z is the direction perpendicular to the electrode surface, the integral is carried over the region of the DL (i.e., from the TIL-DL interface to the DL-bulk interface), and $E(z)$ denotes the scalar z-component of

the electric field. We adopt a convention where a positive (or negative) field corresponds to the air electrode possessing a net positive (or negative) charge. $\chi^{(3)}_{\text{nuc}}$ and $\chi^{(3)}_{\text{elec}}$ are the third-order nuclear and electronic susceptibilities of water. The sum of these two components define the third-order susceptibility of the bulk liquid, *i.e.*, $\chi^{(3)}_{\text{bulk}} \equiv \chi^{(3)}_{\text{nuc}} + \chi^{(3)}_{\text{elec}}$, which has been shown in many previous studies [30, 50, 52, 56] to be a constant for different aqueous interfaces (as long as temperature is not varied and ionic strength < 1M).

The exponential term in Eq. 2 describes the phase sensitivity of the SHG measurement due to mismatch between the DL width (i.e., Debye length) and the wavevector of the incident laser pulse, as denoted by Δk_z and described in detail in Refs.[51, 57-58] This term encodes the effect of interferences between the SHG fields emitted at different depths within the interfacial profile. Typically, the integral in Eq. 2 is expressed in terms of a DC phase angle, $\varphi_{\text{DC}} = \arctan(\Delta k_z \lambda_{\text{D}})$, where λ_{D} is the Debye screening length. Noting that $E(z) = d\Phi(z)/dz$, where $\Phi(z)$ is the electrostatic potential profile, yields the following expression for the real component of the SHG intensity,

$$\left(\chi^{(2)}_{\text{eff}}\right)^2 = \left(\chi^{(2)}_{\text{TIL}} - \Delta\Phi_{\text{DL}}\chi^{(3)}_{\text{bulk}}\cos(\varphi_{\text{DC}})e^{i\varphi_{\text{DC}}}\right)^2 + C \tag{3}$$

where $\Delta\Phi_{\text{DL}}$ denotes the magnitude of the potential drop across the DL. We assume that the potential drop scales linearly with the applied potential, *i.e.*, that $\Delta\Phi_{\text{DL}} = \Delta\Phi_0 + aV_{\text{ext}}$, where $\Delta\Phi_0$ denotes the potential drop across the diffuse layer under unbiased conditions and a is the scale factor that quantifies how much of the applied potential is dropped in the regions between the electrode and the DL (e.g., including the air gap and the TIL). Focusing on the real part of the signal, we arrive at a general model of the SHG intensity,

$$\left(\chi^{(2)}_{\text{eff}}\right)^2 = \left[\chi^{(2)}_{\text{TIL}} - \chi^{(3)}_{\text{bulk}}(\Delta\Phi_0 + aV_{\text{ext}})\cos^2(\varphi_{\text{DC}})\right]^2 + C \tag{4}$$

which predicts a parabolic dependence on V_{ext}.

We assert that $\chi^{(2)}_{\text{TIL}}$ is effectively constant (i.e. negligible variations as compared to that of the DL signal) over the range of fields we apply.[6, 38] We base this assertion on the results of sum frequency generation (SFG) spectroscopy, which reports more precisely on the molecular structure of the TIL. The SFG spectrum of the water interface contains a distinct narrow peak centered around 3700 cm^{-1} that represents the vibration of dangling (unpaired) OH bonds at the surface. Our results, plotted in Fig. 2 (and SI, Figs. S6 – S8), demonstrate that position, shape, and intensity of this peak are invariant to changes in the potential over the range considered in this study (taking into account that SFG probes the OH vibrations as opposed to the electronic transition moment). This invariance reveals that the population of TIL molecules with dangling OH are not affected by the fields we apply and hence the overall molecular structure of the TIL and thus its

SHG contribution is similarly unaffected. This implication is also supported by molecular dynamics simulations, which indicate a negligible change in the orientational distribution of TIL water molecules over the range of field being applied. More specifically, as Fig. 2B illustrates, the fields required to achieve a 10% change in the population of dangling OH molecules are about 10^4-10^5 larger than those we apply in experiment. We also note that despite some build up of hydroxyl ions near the TIL, for example at positive applied potential, the dangling OH remains constant; this is consistent with significantly larger concentrations of hydroxyl ions from prior literature.[59]

If $\chi^{(2)}_{\mathrm{TIL}}$ is independent of applied potential, then the shape of $\left(\chi^{(2)}_{\mathrm{eff}}\right)^2$ versus V_{ext} is given by $\chi^{(3)}_{bulk}$, φ_{DC}, and a. The properties of this shape, *e.g.*, the parabola width, encode details of the influence of external fields on water's interfacial molecular structure. In our analysis we focus primarily on estimating the value of a, which encodes the relationship between V_{ext} and the diffuse layer potential drop, $\Delta\Phi_{\mathrm{DL}}$. To make this estimate, we must make several assumptions about the various terms that appear in Eq. 4. We present a series of physically motivated assumptions and their impact on a in the following section.

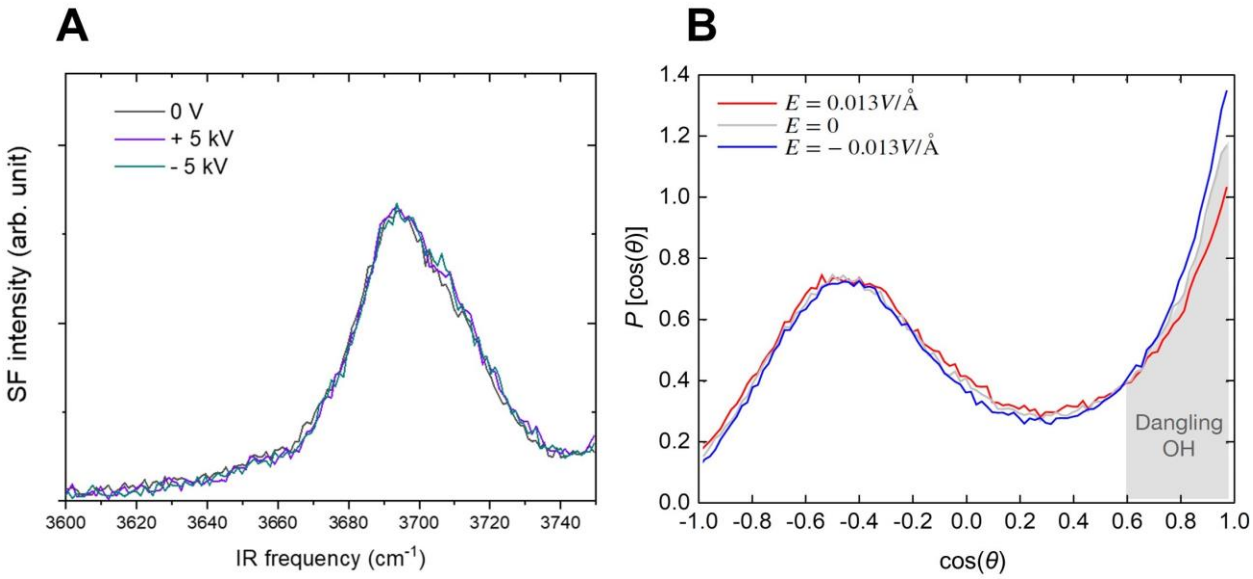

Figure 2. *(A) SFG SSP intensities of water at different potential of -5, 0 and +5 kV showing an invariant dangling OH intensity. (B) Orientational distribution function for water molecules in the first 0.1nm of the neat liquid-water interface from MD simulation under positive and negative fields. The quantity θ represents the angle made between the OH bond vector of a water molecule and the vector normal to the interface pointing towards the vapor phase. We define the fraction of dangling OH molecules as $f_{OH} = \int_{0.6}^{1} P[cos(\theta)]dcos(\theta)$, as indicated by the shaded region. For the plotted distributions $f_{OH}(E = -0.013V/\text{Å})/f_{OH}(E = 0) = 1.08$ and $f_{OH}(E = 0.013V/\text{Å})/f_{OH}(E = 0) = 0.91$. Notably, to achieve*

fields of this magnitude in our system setup would require applied potentials on the order of $10^7 - 10^8$V, many orders of magnitude *larger than those which are applied in our experiment.*

3. **Inferring $\Delta\Phi_{\mathrm{DL}}$ from SHG measurements**

a. Assuming $\varphi_{\mathrm{DC}} = 0$ and $\Delta\Phi_0 = 0$

We begin with the simplifying assumptions that both the DC phase angle and unbiased interfacial potential are equal to zero. *It* is not without justification that we can apply these simplifying assumptions. The DC phase angle, $\varphi_{\mathrm{DC}} = \arctan(\Delta k_z \lambda_{\mathrm{D}})$, arises from interferences of SHG signal at various depths and is thus predicted to be sensitive to changes in the Debye length, λ_D. To probe this sensitivity, we have performed experiments to quantify the SHG intensity change as a function of the ionic strength of the liquid solution (SI, Fig. S5). Our experiments show that SHG intensity is insensitive to the ionic strength. One explanation for this insensitivity is that interferences associated with φ_{DC} are negligible, motivating an assignment of $\varphi_{\mathrm{DC}} = 0$. The assumption that $\Delta\Phi_0 = 0$ can be justified from expectations derived from standard continuum solvent models, such as those based on Poisson-Boltzmann theory. In the absence of external fields, the charge density of the liquid is everywhere neutral eliminating the possibility of a non-zero $\Delta\Phi_{\mathrm{DL}}$.

Assigning $\varphi_{\mathrm{DC}} = 0$ and $\Delta\Phi_0 = 0$ allows Eq. 4 to be reduced to the following form:

$$\left(\chi^{(2)}_{\mathrm{eff}}\right)^2 = \left(\chi^{(2)}_{\mathrm{TIL}} - \Delta\Phi_{\mathrm{DL}}\chi^{(3)}_{\mathrm{bulk}}\right)^2 + C = \left(\chi^{(2)}_{\mathrm{TIL}} - a\, V_{ext}\, \chi^{(3)}_{\mathrm{bulk}}\right)^2 + C \qquad (5)$$

Comparing this equation to the results of experiments allows us to determine how the diffuse layer potential drop changes with V_{ext}. The value of $\Delta\Phi_{\mathrm{DL}}$ is generally some fraction of the overall potential difference applied across the external electrodes. Here, the total potential dropped across the liquid slab (not including that dropped across the air region) is divided equally between the two interfaces, *i.e.*, the air-water and the water-electrode interfaces. Due to screening by the TIL and DL, no potential drop occurs within the bulk region.

The data in Fig. 1B implies that $C = 1.87 \times 10^{-41}\mathrm{m}^2/V^2$. Based on Eq. 5, $\chi^{(2)}_{\mathrm{TIL}}$ can be determined from the value of $\left(\chi^{(2)}_{\mathrm{eff}}\right)^2$ at $V_{\mathrm{ext}} = 0$. This yields $\chi^{(2)}_{\mathrm{TIL}} = -8.67 \times 10^{-22}\mathrm{m}^2/\mathrm{V}$. The sign of $\chi^{(2)}_{\mathrm{TIL}}$ reflects the sign convention we adopted for $E(z)$ and maintains consistency with previous reports in the literature.[10, 25-26, 54] For instance, this convention asserts that the 'hydrogen down' configuration (OH bond vectors oriented into the bulk liquid), which would be favored by positive fields, make a positive contribution to $\chi^{(2)}_{TIL}$. We assign $\chi^{(3)}_{\mathrm{bulk}} = 0.96 \times 10^{-21}\mathrm{m}^2/\mathrm{V}^2$ based on reported literature values.[50] With these values established the

parameter a can be determined by fitting Eq. 5 to the data plotted in Fig. 1B. This fit yields a value of $a = -3.18 \times 10^{-4}$.

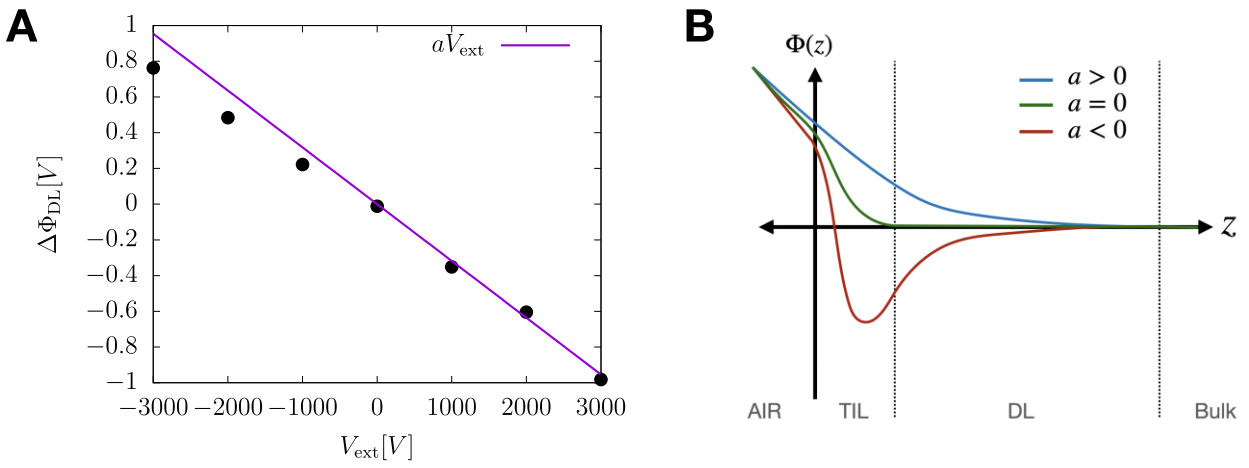

Figure 3. *(A) Dependence of* $\Delta\Phi_{\text{DL}}$ *on applied external potential as determined from Eq. 5 to experimental data (points). Solid line indicates* $\Delta\Phi_{DL} = aV_{ext}$ *with* $a = -3.18 \times 10^{-4}$. *(B) Schematic depictions of electrostatic potential profiles with positive, zero, and negative values of a.*

The two features of a that stand out are its magnitude and sign. Evidently, the potential drop across the diffuse layer is a tiny fraction of the overall device potential drop. Most surprisingly, however, is the result that a is negative in sign, implying that the effective fields in the DL are aligned opposite to expectations based on the external potential. As illustrated in Fig. 3B, this negative value of a would necessitate a non-monotonic potential profile, such as due to overscreening within the TIL and/or the upper boundary of the DL region. We discuss the physical implications of this finding in more detail in the Results and Discussion Section.

b. Assuming $\varphi_{\text{DC}} \neq 0$

To evaluate the effect of non-zero DC phase angle, we consider the dependence of a on φ_{DC} with $\Delta\Phi_0 = 0$. Based on Eq. 4, a non-zero value of φ_{DC} contributes a factor of $0 < \cos^2(\varphi_{DC}) < 1$. The effect of the DC phase angle is thus to amplify the value of a by a factor of $1/\cos^2(\varphi_{DC})$. For example, if $\varphi_{DC} = 13.3°$, as reported in Ref [60], then following the procedure described above for assigning C, $\chi^{(2)}_{\text{TIL}}$, and $\chi^{(3)}_{\text{bulk}}$ yields a value of $a = -3.36 \times 10^{-4}$. Likewise, if $\varphi_{\text{DC}} = 45°$, then $a = -6.37 \times 10^{-4}$. Notably, even with a finite value of φ_{DC}, the value of a is still negative, meaning that all values of φ_{DC} result in an inverse relationship between V_{ext} and the potential drop across the diffuse layer.

c. Assuming $\Delta\Phi_0 \neq 0$

Anisotropy in water orientation and differences in solvation free energies for ions at the interface can cause variations in the electrostatic potential across an interface even under zero external bias. These fields can be quantified and included in the theoretical analysis. Recent studies have reported the value of $\Delta\Phi_0 = -0.49\ V$.[61] To see how a non-zero value of $\Delta\Phi_0$ affects the model prediction, we again assume $\varphi_{DC} = 0$, noting that the influence of this parameter on a will be similar to that described above. Based on Eq. 4, we note that $\Delta\Phi_0$ does not multiply the variable V_{ext} and thus plays a role in renormalizing the leading $\chi_{TIL}^{(2)}$ term. Plugging in $\Delta\Phi_0 = -0.49V$ and fitting to experimental data, retaining the literature value of $\chi_{bulk}^{(3)}$, yields a modified value of $\chi_{TIL}^{(2)} = -1.33 \times 10^{-21}\text{m}^2/V$, notably larger than that derived above. This result is expected since imposing $\Delta\Phi_0 \neq 0$ implies that part of the generally assumed $\chi_{TIL}^{(2)}$ contribution is in reality due to the DL term. Importantly, the value of $a = -3.18 \times 10^{-4}$ is identical to the prediction above. This observation implies that the inverse relationship between V_{ext} and $\Delta\Phi_{DL}$ is not influenced by the unbiased potential drop of the interface.

Using the Poisson Equation and Gouy-Chapman Theory to Predict $\Delta\Phi_{\text{DL}}$

The potential dependence of $\Delta\Phi_{\text{DL}}$ that we infer from Eq. 4 can be contextualized by considering the potential profile that is predicted from the Poisson equation as applied to an electrode-air-water-electrode system. The Poisson equation,

$$\nabla^2\Phi(z) = \frac{\rho(z)}{\epsilon}, \tag{6}$$

relates the electrostatic potential profile to the charge density profile, $\rho(z)$, and the dielectric constant, ϵ. To adapt this equation to our system, we impose two constraints. First, we constrain the potential difference at the system boundaries, i.e., the electrodes, to be equal to the applied potential, V_{ext}. Second, we constrain the potential within the bulk liquid to be constant, due to screening of the TIL and DL. We then determine a charge density profile, $\rho(z)$, that satisfies these two constraints, as described below. From the charge density profile, we can compute the potential profile, $\Phi(z)$.

We assume a quasi-one-dimensional system with two electrodes at positions $z = 0$ and $z = L$, each held at fixed potential. The electrode at $z = L$ sets the reference potential and the electrode at $z = 0$ sets the overall potential drop such that $\Phi(0) = V_{\text{ext}}$ and $\Phi(L) = 0$. The electrode potentials are held fixed by varying the surface charge density of the electrodes, given by the values of $\rho(0)$ and $\rho(L)$. To preserve overall charge neutrality, we assume $\rho(0) = -\rho(L)$. As a first approximation, we divide the region between the electrodes into an air region with $\epsilon = 1$, extending from $0 < z < L/2$, and a water region that we treat

as a uniform continuum with $\epsilon = 80$, extending from $L/2 < z < L$, as illustrated in Fig. 4. To match the experimental system, we define the system size to be $L = 10\text{mm}$.

We model the screening response of the liquid with a Gouy-Chapman-Stern-like model, whereby the potential differences across the liquid slab are screened by the migration of ionic charges to either interface. We include interfacial screening layers in $\rho(z)$ that are symmetric but of opposite charge and that decay to zero over the screening length, λ. As such, $\rho(z) = 0$ in the bulk liquid (i.e., for $L/2 + \lambda < z < L - \lambda$) and in the entire air region (i.e., for $0 < z < L/2$). The screening profile of the water interfaces can be shaped to explicitly differentiate the TIL and the DL regions. The charge density of the electrodes and the net charge density within each screening layer are determined by the two constraints described above.

We perform calculations on the state of the system at the SHG minimum ($V_{ext} = 2.8kV$). We first identify the overall potential drop across the interface, *i.e.*, $\Delta\Phi_{\text{DL}} + \Delta\Phi_{\text{TIL}}$, by modeling the interfacial screening layer as a linear decay in $\rho(z)$ over the screening length as illustrated in Figure 4. We find that for this system architecture, a large majority of the inter-electrode potential drop occurs within the air layer. For instance, at the SHG intensity minimum of $V_{\text{ext}} = 2.8\text{kV}$, only about 200mV is dropped over each liquid interface. As illustrated in Fig. 4D, the excess ion concentration that is required to screen the external potential leads to a net charge density in the DL on the order of 10^{-3}e/nm^3. If screening were carried out purely by hydroxide, this concentration would correspond to excess OH^- concentrations in mM quantities, that is, concentrations that far exceed the bulk value of OH- from autoionization of pure water (~10^{-4} mM).

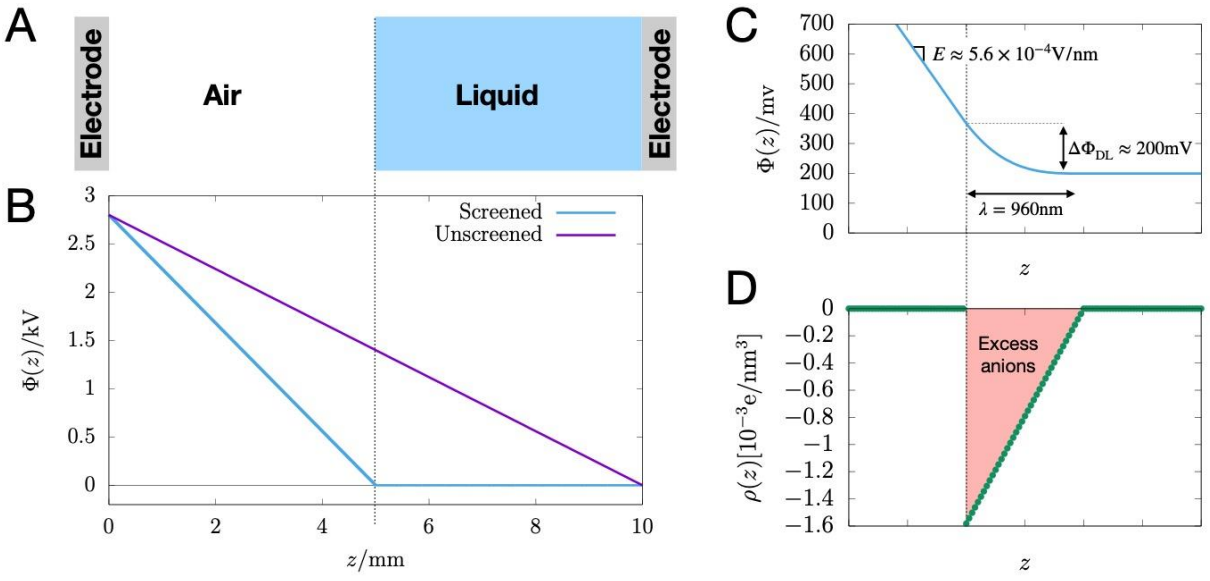

Figure. 4*. Illustrating the electrostatic potential and charge density profiles predicted by the Poisson equation. (A) A schematic of the experimental setup with a variable potential electrode on the left-hand side and a grounded (V=0) electrode on the right-hand side. (B) The formation of a screening layer at both liquid boundaries leads to an attenuation of the potential at the water interfaces, highlighted here at a potential of 2.8kV. As indicated, the fields predicted in these screening regions are significantly larger than that originating from unscreened electrodes separated by vacuum (grey line). (C-D) An illustration of the potential profile and corresponding charge density profile at the water-air interface for positive applied potential. OH^- ions are drawn to the interface by the positive air electrode leading to a diffuse region of excess negative charge.*

The model calculation illustrated in Fig. 4 combines the TIL and DL into a single screening region. Thus, the overall potential drop over this region is divided between the surface layer and the diffuse layer, *i.e.*, $\Delta\Phi_{\mathrm{TIL}} + \Delta\Phi_{\mathrm{DL}} \approx 200\mathrm{mV}$. These components can be separated by representing each explicitly in the charge density profile, $\rho(z)$. To represent the influence of a stratified interfacial density profile on the potential, we solved the Poisson equation for the region of the interface with conducting boundaries at the outer edges of the liquid interface that ensure an overall potential drop of 200mV. We assume that the external field drives an accumulation of charge to the interface in a region between the TIL (which we assumed is neutral in charge) and the DL, which refer to as the surface screening layer (**SSL**). Including such a layer is necessary to arrive at a physically reasonable interpretation of the value $a = -3.18 \times 10^{-4}$. We assume the SSL has a width, d_{SSL} and a uniform charge density of ρ_{SSL}. We model the subsequent diffuse layer with a linearly decaying charge density. Thus, the interfacial charge density profile is given by,

$$\rho(z) = \begin{cases} \rho_{\mathrm{SSL}}, & \text{if } z \in \mathrm{TIL} \\ d(z - z_{\mathrm{bulk}}), & \text{if } z \in DL \end{cases} \qquad (7)$$

where z_{bulk} denotes the position of the DL-bulk interface (located $\lambda = 960\mathrm{nm}$ away from the TIL-DL interface), and d is a constant whose value is determined based on the condition that the overall potential drop is equal to 200mV.

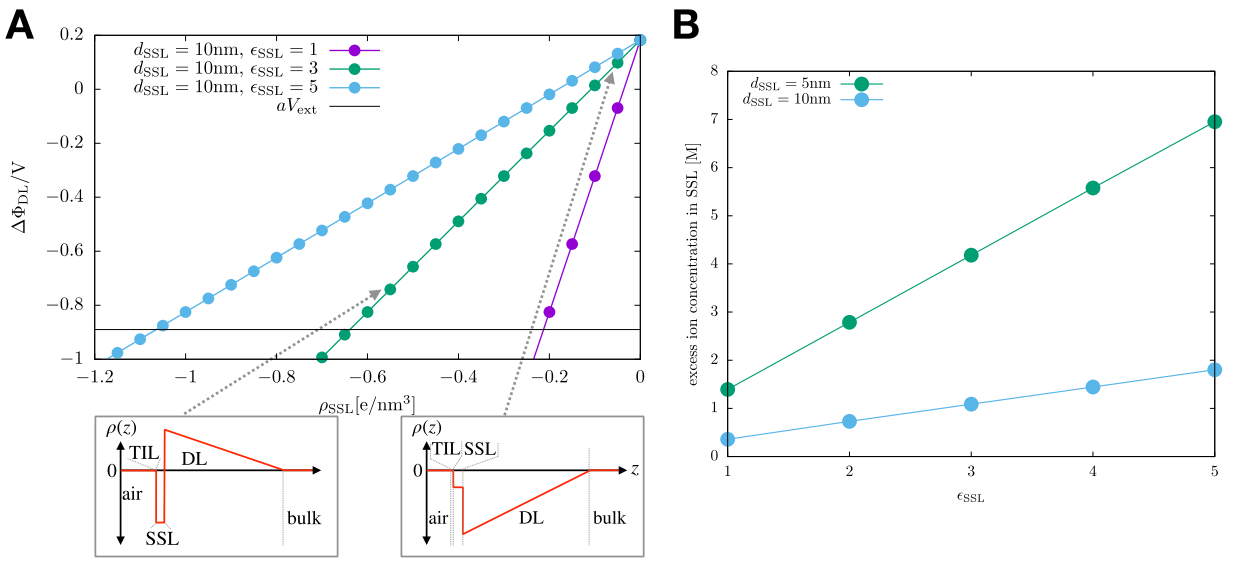

Figure 5. *(A) Modeling results that illustrate the dependence of* $\Delta\Phi_{\mathrm{DL}}$ *on the excess charge density within the surface screening layer, SSL (*ρ_{SSL}*) for an overall interfacial potential drop of* $\Delta\Phi_{TIL} + \Delta\Phi_{DL} = 200mV$ *(i.e., corresponding to* $V_{ext} = 2.8kV$*). The value of* $\Delta\Phi_{\mathrm{DL}}$ *depends on the assumed dielectric of the SSL. The lower the dielectric constant, the more effective the screening. For an SSL with 10nm width and* $\epsilon = 3$*, the negative values of* $\Delta\Phi_{\mathrm{DL}}$*, such as inferred from analyzing experimental results with Eq. 3, require excess anion concentrations within the SSL of approximately 1M. Although, if one assumes an interfacial dielectric of 1 (a reasonable assumption) and with the same SSL of 10 nm, the ion build up is around 350 mM. Lower panels of* ***A*** *contain schematic illustrations of the charge density profile at large and moderate SSL concentrations. (B) The value of excess ion concentration in the SSL required to achieve* $\Delta\Phi_{\mathrm{DL}}$*=-0.89V for different SSL widths and dielectric constants. When the SSL is more narrow, higher concentrations are required to achieve overscreening. Excess ion concentration in the SSL varies dramatically for with SSL assumptions.*

The results of this calculation when $V_{\mathrm{ext}} = 2.8\mathrm{kV}$ and $d_{SSL} = 10nm$ for a range of values of ρ_{SSL} are illustrated in Fig. 5. We compare these results to the expectation derived in Sec. 3a, that when $V_{\mathrm{ext}} = 2.8\mathrm{kV}$, $\Delta\Phi_{\mathrm{DL}} = aV_{ext} = -0.89V$. We find that to achieve agreement between the experimental data and the Poisson equation model, the charge density of the SSL must be $\rho_{\mathrm{TIL}} \approx 0.64\mathrm{e/nm}^3$, roughly corresponding to an excess ionic concentration of 1M within the SSL of dielectric 3, although reducing to 350mM in the example of a dielectric of 1 at the interface. The excess ion concentration in the SSL required for consistency with the experimental data in Fig. 1 depends sensitively on the assumed characteristics of the SSL. Figure 5 illustrates this sensitivity in two ways. In Fig. 5A we plot the dependence of $\Delta\Phi_{DL}$ on ρ_{SSL} for several different values of the SSL dielectric. Intuitively, increasing the dielectric constant of the SSL

reduces the slope of the curves. Figure 5B shows how the value of ρ_{SSL} needed for experimental consistency depends on d_{SSL} and ϵ_{SSL}. A narrower SSL requires a larger excess ion concentration to achieve the same screening effect. At $d_{SSL} = 1nm$ and $\epsilon_{SSL} = 3$, the excess ion concentration needed is an entirely unphysical 60M.

Consequences for our fundamental understanding of the electrical double layer

The model results plotted in Fig. 5 suggest that at the minimum SHG intensity ($V_{\text{ext}} = 2.8\text{kV}$) the interface develops an overscreening layer (the SSL) that is probably several nm thick. Under the conditions of the experiment, this overscreening layer is much narrower than the adjacent diffuse layer, which thus contributes to the potential dependence of the SHG intensity through $\chi^{(3)}_{\text{bulk}}$. Notably, however, this physical picture is unexpected and difficult to justify based on standard physical intuition. The development of a SSL with low associated dielectric constant would have other physical and mechanical implications that presumably would have manifest in previous studies of this ubiquitous system.[62]

Thus, we propose that the erroneous assumption is either in the appropriateness of the Poisson model in describing this system or in the theoretical basis underlying the use of Eq. 3 for interpreting SHG experiments. While we lack the current capability to distinguish between these two options, we discuss each briefly below.

What does the Poisson model omit? In the standard Poisson model, as we present above, it is assumed that screening is entirely governed by the ionic density profile. However, solvent polarization (both electronic and nuclear) can also contribute significantly to the screening properties of the water interface. For example, classical simulations of neat water-electrode systems show that preferential orientations of water molecules at an unbiased electrode-water interface can lead a significant potential drop (roughly -1V for point-charge force fields) over the first 1nm of the interface. This potential drop is a consequence of the orientational forces that arise due to strong water-metal interactions and thus cannot be predicted from the Poisson equation alone. The Poisson/Gouy-Chapman model also idealizes the composition and geometry of the system. For example, the screening length we assume does not include possible effects of impurities, such as carbonate ions.

What does Equation 4 omit? The derivation of Eq. 4 is based on the assumption that changes to the SHG response of the DL are the direct influence of the external field on the molecular structure of the DL. The external field also affects the composition of the DL by imbalancing the anion/cation ratio, as well as local fields that go beyond the solvation shell. These imbalances could potentially lead to SHG-active solvent configurations, e.g., due to asymmetric solvation shells for OH- adopting particular orientations near the

interface. As a proof of concept, we can include these hypothetical *mechanical solvation effects* by including an additional term in the equations.

To see how these hypothetical mechanical effects would modify the theoretical formalism for describing potential dependent SHG intensity, we add a term that quantifies the effect. Starting from Eq. 2,

$$\chi_{DL}^{(2)} = \chi_{\text{bulk}}^{(3)} \int_{DL} \left(E(z) e^{i\Delta k_z z}\right) dz + \int_{DL} \alpha \frac{d\rho(z)}{dz} d \\ = -\chi_{\text{bulk}}^{(3)} (\Delta\Phi_0 + \text{aV}_{ext}) \cos(\varphi_{DC})^2 - \alpha\rho_{DL} \tag{8}$$

where we have assumed here that the mechanical contribution to $\chi_{\text{DL}}^{(2)}$ depends on the local gradient in the ionic imbalance and the relative strength of the effect is parameterized by α. The gradient dependence implied here would be appropriate if, for example, the mechanical effect arose from an imbalance between the concentration of hydrogen bond donating and accepting ions. An alternate z-dependence can be assumed to account for other physical effects. In the second equality, ρ_{DL} denotes the net charge density at the boundary between the TIL and the DL. Assuming that anions and cations have charges $-q$ and q, we can expand $\alpha\rho_{DL}$ as,

$$\alpha\rho_{DL} \approx \alpha\rho_0 \left(e^{-\beta q \Delta\Phi_{\text{DL}}} - e^{\beta q \Delta\Phi_{\text{DL}}}\right), \tag{9}$$

where ρ_o is the bulk concentration of anions (or cations). Assuming that $\beta q \Delta\Phi_{\text{DL}} \ll 1$, we end up with,

$$\alpha\rho_{DL} \approx -2\alpha\rho_0 \beta q \Delta\Phi_{\text{DL}} \equiv -\rho_0 \Delta\Phi_{\text{DL}} \chi_{\text{mech}}^{(3)} \tag{10}$$

leading to an expanded version of Eq. 3.

$$I \propto \left[\chi_{TIL}^{(2)} + \Delta\Phi_{\text{DL}} \left(\chi_{\text{bulk}}^{(3)} - \rho_0 \chi_{\text{mech}}^{(3)}\right)\right]^2 \tag{11}$$

According to this expression, the magnitude of the mechanical effect can be inferred from the dependence of SHG intensity on ionic strength. Notably, the form of this equation depends on the assumed position dependence of the mechanical effect. If the effect was directly proportional to $\rho(z)$ (rather than on its gradient), or was isolated to the TIL/DL boundary, the expression in Eq. 9 - 11 would take a different form, with different ionic strength dependence.

Conclusion

Our combined experimental and theoretical study provides new insight into the screening properties of the diffuse layer at the air-water interface under externally applied electric fields. Our experiments reveal a

parabolic dependence of SHG intensity on applied field strength, with a minimum intensity at positive fields as generated by an external electrode held at a potential of 2.8kV relative to the ground. We interpret this parabolic profile with a model of water's second harmonic response that includes a static second-order susceptibility arising from the surface layer of water molecules, and a potential dependent second-order susceptibility arising from the diffuse layer separating the surface and the bulk. This interpretation leads to the counterintuitive conclusion that overall potential change across the diffuse layer of the interface is small but a negative fraction of that is dropped across the liquid slab. We evaluate this conclusion in the context of traditional models of electrolyte screening and determine that the overscreening to yield such a negative fraction would require a massive concentration of ion buildup within the TIL and/or the upper boundary of the DL. Together, the observation, interpretation, and modeling yield a physical picture that goes beyond the traditional model of the electric double layer. In particular, we conclude that at least one of the following must be true: (i) ion enrichment at the interface goes beyond pure electrostatics and is also driven by preferential solvation, (ii) solvent polarization contributes to the screening, which is not taken into account in the Poisson model, (iii) local fields generated by the imbalance of the anion/cation ratio within the EDL locally dominates over the externally applied field and dictates water orientation distributions at the interface. Resolving these identified contributions in future studies will help solidify our understanding of this ubiquitous and fundamental system and improve our comprehension of electric double layers.

Methods:

1.0 Materials and Sample Preparation

Milli-Q (>18.0 MΩ) ultra-pure water was used as a neat water source without the addition of any other chemicals. The purity of the neat water was confirmed by measuring the surface tension of water. Our measurements of (72.15±0.08) mN/m at (23.1±0.5)°C are in agreement with previous literature.[63-64] The pH was monitored; before the experiment, between 5-15 minutes after obtaining water from our Milli-Q system, the pH was measured to be 6.29 ± 0.05 at (23.1 ± 0.5)°C (Table S1). The pH of water then dropped to (5.80 ± 0.08) after 5 to 6 hours of atmospheric exposure due to CO_2 absorption as is expected. Second harmonic measurement began 30 mins after obtaining the water samples from the Milli-Q system. Applied voltage experiments were completed over an ~5.5 to 6.5 hour time period in which sample height was adjusted to maintain alignment. The observed decrease of pH with time was shown to be undetectable by second harmonic measurement; reversing the order and randomization of experiments verified this conclusion, among other controls.

1.1 Second Harmonic Generation

1.1.1 Instrumentation and experimental setup. A custom-built Second Harmonic Generation system was utilized for these experiments (Fig. S1). The SHG system consists of a Ti:sapphire oscillator (Tsunami, Spectra-Physics, average power output of 860 mW) with a wavelength centered at 805 nm, a half width half maximum of 10 nm, a sub 50 fs pulse width, and a repetition rate of 82 MHz with a power density of 10^{10} W/cm^2 calculated using the measured 550 mW at the sample stage from a focused 805 nm beam (75 mm FL). Note that water ionization is neglected due to low power densities (10^{14} W/cm^2 are typical of ionization through multiphoton absorption processes).[65] The oscillator is pumped by a continuous wave (CW) solid state diode laser (Millennia Vs, Spectra-Physics) with a pump power of 5 W. The output laser beam is separated by a ratio of 90/10 by a beam splitter, where 90% of the laser power is introduced to the sample channel and the other 10% of the beam is used in the reference channel (BBO nonlinear optical crystal). The sample channel consists of four dielectric mirrors (BB1-E03, Thorlabs), one Glan-laser polarizer (10GL08AR.16, Newport), one half-wave plate (10RP52-2B, Newport), one plano-convex lens with a focal length of 75 mm (LA1608-B, Thorlabs) and one 690 nm long-pass filter (690LP RapidEdge, Omega Optical). The laser pulses reflect off of the liquid surface with an angle of 67.2° with respect to the surface normal and collected with typically 180 second accumulated acquisitions.

The detection system is comprised of a Czerny-Turner type monochromator (Shamrock SR303i, Andor Tech.) and an EMCCD (Newton DU970N-BV EMCCD, Andor Tech.). The monochromator grating is 68x68 mm with a groove density of 300 lines/mm. The CCD consists of 1600x200 pixel array (Blazed at 500 nm), with 16x16 µm pixel size. Electron multiplying was set to 200 times to enhance the signal count and the thermal electric cooling was set at -60 °C to reduce thermal noise.

The high voltage set up is comprised of two electrodes: the DC-powered steel electrode (25x20 x0.40 mm^3), located in the air-phase, and the grounded parallel platinum counter electrode (25x22x0.10 mm^3, Fisher Scientific) in the condensed-phase. The applied external potential range was negative (-) 5 to positive (+) 5 kV, where the applied electric field was normal to the water-air interface. The distance between the air-phase electrode and the water surface was maintained at 5 mm, whereas the condensed-phase electrode was maintained at 5 mm below the water surface for fixed airgap experiments. Additional SHG control experiments were carried out at varying relative humidities (ranged from 20% to 40%RH) and with N_2 purging within the experimental sample area; the acquired data was consistent with unpurged data as presented in this manuscript. The effect of the external potential on the water-air interface was also studied by changing the airgap between the water surface and the air-electrode from 5 mm to 27 mm with a constant external potential of +3 kV.

Note that additional details are discussed in the SI.

1.1.2 Vibrational Sum Frequency Generation Spectroscopy

The details of the broadband sum frequency generation spectrometer set up used for this study were previously reported.[66-68] In brief, a regenerative Ti:sapphire amplifier (Spitfire Ace, Spectra-Physics) seeded with a sub-50 fs 800 nm pulse from a Ti:sapphire oscillator provides an ~3.5 W beam of 75 fs pulses and 1 kHz repetition rate. The amplified beam is then directed through a 50:50 beam splitter. One half of the beam is used to pump an optical parametric amplification system (TOPAS-C, Light Conversion), that is coupled to a non-collinear difference frequency generator (NDFG, Light Conversion) to generate the broadband infrared beam. The other half of the beam is spectrally narrowed to a FWHM of 12 cm^{-1} by an etalon (SLS Optics, United Kingdom) and is used as the visible 797 nm beam. The infrared and the visible beams are co-propagating and fall on the sample surface at angle from the surface normal of 60 and 50 degrees, respectively. The visible beam is focused approximately 1 cm after the surface with a BK7 lens (25 cm FL) and the infrared beam is focused on the sample surface with a CaF_2 lens (15 cm FL). The sum frequency signal is collected in the reflected direction by a spectrometer (IsoPlane SCT 320, Princeton Instruments) and a liquid nitrogen cooled CCD (PyLoN, 1340 × 400 pixels, Princeton Instruments). The IR laser profile and energies of visible and IR beam were periodically measured and was stable throughout the measurement. The polarization combinations used in the sum frequency experiments were PPP and SSP are listed in the order of decreasing frequency (SF, Vis, IR). Light polarized perpendicular to the incident plane is referred to as S polarized, whereas light polarized parallel to the incident plane is P polarized. The vibrational modes that contribute to a particular polarization combination depend on the polarization of the infrared field and the direction of the infrared and Raman transition moments. The SSP polarization combination accesses vibrational modes primarily with dipole transition moments that have components perpendicular to the surface plane. Whereas, vibrational modes with components that are both perpendicular and parallel to the surface plane will be present in PPP polarization.[66]

1.1.3 Second Harmonic Intensity and Nonlinear Susceptibility. Given that the SHG data is being modeled, we further describe the relevant details here. The second harmonic intensity of the water-air interface was collected using the custom built second harmonic instrument described above using PP polarization. (Other polarization data shown in the SI.) The reflected second harmonic signal intensity, $I(2\omega)$, on the neat water surface can be written in terms of the incoming laser intensity, $I(\omega)$, as follows:[69-71]

$$I(2\omega) = \frac{32\pi^3\omega^2 \sec^2\beta}{c_0^3 n_1(\omega) n_1(\omega) n_1(2\omega)} \left|\chi_{eff}^{(2)}\right|^2 I^2(\omega) \qquad (12)$$

Where, c_0, $n_i(\omega_i)$ and β denote the speed of light in vacuum, refractive index of the medium, and incident angle of the incoming laser normal to the water surface, respectively. Here, $\chi_{eff}^{(2)}$ indicates the effective second-order susceptibility of the water surface. The effective second-order susceptibility data of water at different external potentials and polarization are presented as Fresnel-removed second order susceptibilities in Fig. S9 (Details in SI section 2 and 3).

The dependence of second harmonic signal intensity on surface potential and surface charges are well established and related to the bulk $\chi^{(3)}$.[56, 72-76] This third-order contribution was first reported at the silica/water interface using second harmonic generation by Eisenthal *et al.*[72] EFISH predates this finding as a method for bulk $\chi^{(3)}$ determination.

2.1 Replicate and Control Experiments

2.1.1 Replicate Second Harmonic Measurements with Applied Potentials. Replicate measurements on water surface were performed under P in P out and 45 in S out polarization with the applied external potentials ranging from negative (-) 5 kV to positive (+) 5 kV by keeping a fixed airgap of 5 mm (Fig. S2 and S3). A minimum of six replicate measurements were performed for each data point presented. Here, we show six and two separate sets of experiments of P in P out and 45 in S out polarization data, respectively, to justify the robustness of the measurements. The measured data show higher and lower potential under negative and positive external potential, respectively, where the trends show similar behavior with the data presented in Fig. 1B. Moreover, the replicate measurements show a parabolic shape with minimum intensity at +2.8 kV. The measurements at individual external potential show highly reproducible data with negligible variation (~5% to 8%).

2.1.2 Applying a Fixed Potentials with Varying Airgap: Second Harmonic Response. The variation of the water surface second harmonic intensity was investigated under a fixed external potential (+3 and -3 kV) with varying airgaps ranging from 0.5 to 2.7 cm. The airgap was defined as the distance between the water surface and the air-electrode. We observe a monotonic decrease in experimental signal intensity with increasing separation distance between the air electrode and the water interface with an associated decrease in electric fields (Fig. S4**)**.

3 Theory

3.1.1 Sign of the TIL contribution to SHG. While the SHG activity of the TIL is due to its molecular structure, intrinsically different from the bulk, $\chi_{\mathrm{DL}}^{(2)}$ intensity solely depends on the static electric field across the interfacial DL region and is proportional to the potential difference across the DL (Φ_{DL}). A number of

previous studies have shown that $\chi^{(2)}_{\mathrm{TIL}}$ at the water-air interface only exhibits small changes with respect to variations in pH and ion concentration,[5, 77-80] while much larger variations are observed for $\chi^{(2)}_{\mathrm{DL}}$. However, the sign of $\chi^{(2)}_{\mathrm{TIL}}$ still plays a key role in determining Φ_{DL} from measured SHG activities. Despite the measured SHG signal does not give information on the sign of $\chi^{(2)}$ ($I(V) = \left|\chi^{(2)}\right|^2$), the sign of $\chi^{(2)}_{\mathrm{TIL}}$ can be assigned from the knowledge of the water dipole orientation within the TIL, as discussed in the text: $\chi^{(2)}_{\mathrm{TIL}}$ has positive sign. Knowing this, we can also assign the sign of $\chi^{(2)}$ (and therefore of the extracted values of Φ_{DL}), based on the following considerations.

The minimum SHG intensity is measured at positive applied potential of V=2.8 kV. This implies that:

- $\chi^{(2)}_{\mathrm{TIL}}$ and $-\chi^{(3)}_{\mathrm{bulk}}\Phi_{\mathrm{DL}}$add up for $V < 0V$.
- $\chi^{(2)}_{\mathrm{TIL}}$ and $-\chi^{(3)}_{\mathrm{bulk}}\Phi_{\mathrm{DL}}$ compensate each other for $V > 0V$.

Therefore, $\chi^{(2)} = \sqrt{I(V)}$ has the same sign as $\chi^{(2)}_{\mathrm{TIL}}$ for negative V values and changes sign at 2.8 kV:

$$+\chi^{(2)}, \qquad if\ V < 2.8\ kV$$

$$-\chi^{(2)}, \qquad if\ V > 2.8\ kV$$

3.1.2 Gaussian Field Model. The characteristic feature of the experimental results in this system is a minimum in the spectroscopic response of the air-water interface at a non-zero applied field. Here, we sketch a simple Gaussian model for the interfacial polarization field that provides a compelling microscopic interpretation of the experimental result. It is known and well accepted that even under zero applied potential, water molecules at the air-water interface carry an intrinsic polarization due to broken longitudinal symmetry at the interface. To low order, we expect fluctuations around the preferred polarization at any field to carry Gaussian statistics.

Equipped with these physical considerations, we postulate the following Hamiltonian for the z-component of the polarization variable $\pi_z$at the interface,

$$H[\pi_z] = \frac{k}{2}[\pi_z - \pi_z^*]^2 - \lambda \cdot \pi_z E_z \tag{13}$$

where π_z is the z-component (taken as normal to the interface by convention) of the plane-averaged dielectric polarization at the interface, π_z^* is the preferred value of the polarization at zero applied field, k is the energy scale associated with interfacial polarization fluctuations, E_z is the z-component of the applied interfacial electric field, and λ is a coupling constant quantifying the tendency of the applied electric field to align water dipoles at the interface. Mathematically, adding a linear coupling to a parabolic Hamiltonian simply translates the parabola to a new preferred polarization value. Completing the square results in an equivalent expression for the Hamiltonian that makes this field-dependent shift in the preferred polarization obvious,

$$H[\pi_z] = \frac{k}{2}\left[\pi_z - \left(\pi_z^* - \frac{\lambda E_z}{k}\right)\right]^2 - \lambda E_z\left(1 + \frac{\lambda E_z}{2k}\right) \tag{14}$$

At this point, we address units. For the sake of easily estimating parameters from molecular simulation, we track the polarization field π_z in fictive $\cos\theta$ units. One can glean the quantity in these units by normalizing the interfacial polarization vector by an arbitrary polarization scale, and then dotting the normalized vector into the interface normal. The Hamiltonian above is Gaussian, and so we can simply read off the mean from the offset in the quadratic term. Specifically, the mean polarization goes as,

$$\langle \pi_z \rangle = \pi_z^* - \frac{\lambda E_z}{k} \tag{15}$$

The spectroscopic response of the interface is proportional to the square of the mean interfacial polarization, plus any background signal,

$$\text{Response}[E_z] = B + A \cdot \langle \pi_z \rangle^2 \tag{16}$$

where B is the magnitude of background signal, and A is a proportionality constant relating the interfacial polarization to the spectroscopic response, both of which are assumed to be constant at all values of the applied interfacial field. Since the experimental data is normalized to the zero-field value, we can factor out the background response and eliminate it as an overall constant, leaving us with,

$$\text{NormResponse}[E_z] = 1 + \left(\frac{A}{B}\right) \cdot \left[\pi_z^* - \left(\frac{\lambda}{k}\right) E_z\right]^2 \tag{17}$$

where the response carries a parametric dependence on the quantities π_z^*, λ/k , and A/B, which need to be estimated from simulation data.

First, the quantity $\langle \pi_z \rangle$ simply serves to scale the interfacial polarization into spectroscopic signal, and is assumed to be independent of the applied field. Since we can only access the value of $\langle \pi_z \rangle$ directly from simulation data, without loss of generality, we set $A/B = 1$. We choose to estimate the remaining model parameters, π_z^*, and λ/k using insight provided by simulations of an interface between water and a perfectly volume-excluding wall that can carry a surface charge. The surface charge density at the wall, σ_q, can be mapped to an effective interfacial electric field in the simulation data. Fig. S10 shows a relationship between the surface charge density at the wall (measured in arbitrary units) vs. the computed interfacial electric field (in units of V/Å). The slope gleaned from this linear relationship is 0.65 V/Å, implying that the interfacial electric field increases by 0.65 V/Å for each σ_q unit.

As worked out in the section above on field magnitudes, the maximal applied experimental field is roughly 0.44 V/Å. Hence, simulations conducted with wall charge densities up to $\sigma_q \approx 0.68$ are in correspondence with the experimental field magnitudes. Trajectory analysis on the molecular dynamics simulation data allows for quantification of the orientational distributions of water molecules, resolved as a function of distance from the interface. Fig. S11A shows distributions of the interfacial polarization as a function of the wall charge density σ_q. Fig. S11B shows the modal value of the interfacial polarization as a function of σ_q. We choose to use the mode as a summary statistic for the distribution because it is more robust to the large tails of the distributions easily identifiable in Fig. S11A.

With the data in these two plots in hand, we estimate the values of the model parameters. The parameter λ/k describes how much the preferred polarization value moves with the applied interfacial field. If we employ the modal value of the $\cos\theta$ distribution as a proxy for the preferred polarization value and estimate the interfacial electric field in units of σ_q, then we can estimate λ/k from the data available in Fig. S11B. Specifically, λ/k is the slope of the response curve; we have a decision to make as to the range of σ_q values over which we fit this response slope. If we choose the dynamic range of $\sigma_q \in [-0.1, 0.1]$ for slope estimation from Fig. S11B, then we have $\lambda/k \approx 0.75$ in the aforementioned units. We can estimate the value of π_z^*, by examining the modal value of the interfacial polarization at zero externally applied field. Reading off the value at $\sigma_q = 0$ in Fig. S11B yields the estimate $\pi_z^* \approx 0.18$.

The typical length scale associated with the hydrogen bonding network of water is $L_{\mathrm{scl}} = 1$ nm. Hence, by a simple scaling argument, the typical magnitude of electric field fluctuations associated with rearrangements of the hydrogen bond network is,

$$E_{\mathrm{scl}} = \frac{k_{\mathrm{B}}T}{eL_{scl}} \approx 2.5 \times 10^{-3} \frac{V}{\text{Å}} \tag{18}$$

3.1.3 Models for Experimental Field Magnitudes. In the experimental apparatus, the applied voltage between two parallel plates can reach as high as 5 kV. Naively, if we were to drop this entire voltage over the 5 mm water layer as if in a parallel-plate capacitor, we would obtain a paltry (on a molecular scale) field of $E \approx 1 \times 10^{-4}$ V/Å. Insights from simulation data, and simple thermodynamic arguments (the field is far lower than the thermal field $E_{\mathrm{thermal}} = k_{\mathrm{B}}T/[e \times 1\ \text{Å}]$) suggest that the field experienced at the interface is orders of magnitude greater than this simple parallel-plate capacitor argument may suggest.

We advance the hypothesis that elevated interfacial fields are present in the experiment due to formation of an electrical double-layer near the air-water interface by the hydronium and hydroxide ions present in water at the experimental pH. The experiment is conducted at pH = 6.25, implying a hydronium concentration $c_{\mathrm{Hydronium}} = 5.6 \times 10^{-7}\mathrm{mol/L}$ and a hydroxide concentration $c_{\mathrm{Hydroxide}} = 5.6 \times 10^{-7}\mathrm{mol/L}$. The relevant length scale for formation of an electrical double layer is the Debye length,

$$\ell_{\mathrm{Debye}} = \left[\frac{\epsilon k_{\mathrm{B}}T}{\sum_j c_j q_j^2}\right]^{1/2} \tag{19}$$

where ϵ is the dielectric constant of neat water, k_{B} is the Boltzmann constant, T is the temperature, the sum runs over all ionic species j, and c_j and q_j denote the concentration and charge carried by the ionic species, respectively. At the experimental conditions, the Debye length is $\ell_{\mathrm{Debye}} = 565$ nm. If we assume that half the potential drop is dropped over the air-water double-layer (the other half is dropped over the grounded electrode-water double layer), then the maximal accessible interfacial field in experiment is roughly 0.44 V/Å.

3.2 Molecular Dynamics Simulation Methods. The molecular dynamics simulations employed in this work model water molecules using an atomistic molecular mechanics force field. The water molecules are in contact with an idealized wall of volume-excluding spheres carrying a constant surface charge, which is variable across different simulations. Orientational statistics of water molecules are computed relative to the local instantaneous interface, a construct developed by Willard and Chandler which factors out long-wavelength capillary wave-like fluctuations from the interface.[81] The distributions and values of order parameters from simulations presented in Figs. S11A and S11B are time averages taken over an entire trajectory of simulation.

Acknowledgments: "This work was supported by the U.S. Department of Energy, Office of Science, Basic Energy Sciences, under Awards # DE-SC0016381 and # DE-SC0018094, Allen and Willard Labs, respectively. HCA and KKR acknowledge Prof. A. Co for helpful discussions. S.P. acknowledges financial support by the Deutsche Forschungsgemeinschaft (DFG, German Research Foundation) under Germany's Excellence Strategy EXC2033-390677874-RESOLV and by the European Research Council (ERC) Advanced Grant 695437 THz-Calorimetry.

Author contributions:

¥ K.K.R. and A.L. contributed equally to this work. H.C.A conceived of the laboratory studies; A.P.W. conceived of the theoretical analysis; K.K.R. and K.C.N. designed the SHG set up and experiments. K.K.R. carried out SHG experiments. A.L. performed calculations and MD simulations. A.S. and K.K.R. performed sum frequency generation (SFG) characterization. A.P.W., S.P., and M.P.G. contributed the modeling of SHG activity in terms of the potential change across the interface. A.P.W. and H.C.A wrote the manuscript with help from all the authors.

Competing Interests

The authors declare no competing interests.

Additional information

Extended data is available for this paper at _____

Supplementary information is available for this paper at _...

Correspondence and requests for materials should be addressed to H.C.A and A.P.W. for experimental and theory detail, respectively.

Peer review information *PNAS* thanks the anonymous reviewers for their contribution to the peer review of this work.

Reprints and permissions information is available at …

References

1. Ohmine, I.; Tanaka, H., Fluctuation, relaxations, and hydration in liquid water. Hydrogen-bond rearrangement dynamics. *Chem. Rev.* **1993,** *93* (7), 2545-66.
2. Ohmine, I.; Saito, S., Water Dynamics: Fluctuation, Relaxation, and Chemical Reactions in Hydrogen Bond Network Rearrangement. *Acc. Chem. Res.* **1999,** *32* (9), 741-749.
3. Smith, J. D.; Cappa, C. D.; Wilson, K. R.; Messer, B. M.; Cohen, R. C.; Saykally, R. J., Energetics of Hydrogen Bond Network Rearrangements in Liquid Water. *Science* **2004,** *306* (5697), 851-853.
4. Nicodemus, R. A.; Corcelli, S. A.; Skinner, J. L.; Tokmakoff, A., Collective Hydrogen Bond Reorganization in Water Studied with Temperature-Dependent Ultrafast Infrared Spectroscopy. *J. Phys. Chem. B* **2011,** *115* (18), 5604-5616.
5. Goh, M. C.; Hicks, J. M.; Kemnitz, K.; Pinto, G. R.; Heinz, T. F.; Eisenthal, K. B.; Bhattacharyya, K., Absolute orientation of water molecules at the neat water surface. *J. Phys. Chem.* **1988,** *92* (18), 5074-5.
6. Gopalakrishnan, S.; Liu, D.; Allen, H. C.; Kuo, M.; Shultz, M. J., Vibrational spectroscopic studies of aqueous interfaces: salts, acids, bases, and nanodrops. *Chem. Rev.* **2006,** *106* (4), 1155-75.
7. Jungwirth, P.; Finlayson-Pitts, B. J.; Tobias, D. J., Introduction: Structure and Chemistry at Aqueous Interfaces. *Chem. Rev.* **2006,** *106* (4), 1137-1139.
8. Shen, Y. R.; Ostroverkhov, V., Sum-frequency vibrational spectroscopy on water interfaces: polar orientation of water molecules at interfaces. *Chem. Rev.* **2006,** *106* (4), 1140-54.
9. Benjamin, I., Reaction dynamics at liquid interfaces. *Annu. Rev. Phys. Chem.* **2015,** *66*, 165-188.
10. Nihonyanagi, S.; Kusaka, R.; Inoue, K.-i.; Adhikari, A.; Yamaguchi, S.; Tahara, T., Accurate determination of complex χ(2) spectrum of the air/water interface. *J. Chem. Phys.* **2015,** *143* (12), 124707/1-124707/4.
11. Sitzmann, E. V.; Eisenthal, K. B., Picosecond dynamics of a chemical reaction at the air-water interface studied by surface second harmonic generation. *J. Phys. Chem.* **1988,** *92* (16), 4579-80.
12. Benjamin, I., Theoretical study of ion solvation at the water liquid-vapor interface. *J. Chem. Phys.* **1991,** *95* (5), 3698-709.
13. Jungwirth, P.; Tobias, D. J., Surface effects on aqueous ionic solvation: A molecular dynamics simulation study of NaCl at the air/water interface from infinite dilution to saturation. *J. Phys. Chem. B* **2000,** *104* (32), 7702-7706.
14. Kuzmenko, I.; Rapaport, H.; Kjaer, K.; Als-Nielsen, J.; Weissbuch, I.; Lahav, M.; Leiserowitz, L., Design and Characterization of Crystalline Thin Film Architectures at the Air−Liquid Interface: Simplicity to Complexity. *Chem. Rev.* **2001,** *101* (6), 1659-1696.
15. Culp, J. T.; Park, J.-H.; Stratakis, D.; Meisel, M. W.; Talham, D. R., Supramolecular Assembly at Interfaces: Formation of an Extended Two-Dimensional Coordinate Covalent Square Grid Network at the Air−Water Interface. *J. Am. Chem. Soc.* **2002,** *124* (34), 10083-10090.
16. Garrett, B. C., Chemistry. Ions at the air/water interface. *Science* **2004,** *303* (5661), 1146-1147.
17. McFearin, C. L.; Richmond, G. L., The Role of Interfacial Molecular Structure in the Adsorption of Ions at the Liquid-Liquid Interface. *J. Phys. Chem. C* **2009,** *113* (50), 21162-21168.
18. Neal, J. F.; Zhao, W.; Grooms, A. J.; Smeltzer, M. A.; Shook, B. M.; Flood, A. H.; Allen, H. C., Interfacial Supramolecular Structures of Amphiphilic Receptors Drive Aqueous Phosphate Recognition. *J. Am. Chem. Soc.* **2019,** *141* (19), 7876-7886.
19. Conway, B. E.; Bockris, J. O. M.; Ammar, I. A., Dielectric constant of the solution in the diffuse and Helmholtz double layers at a charged interface in aqueous solution. *Trans. Faraday Soc.* **1951,** *47*, 756-66.
20. Shiratori, K.; Morita, A., Molecular theory on dielectric constant at interfaces. A molecular dynamics study of the water/vapor interface. *J. Chem. Phys.* **2011,** *134* (23), 234705/1-234705/10.
21. Dinpajooh, M.; Matyushov, D. V., Dielectric constant of water in the interface. *J Chem Phys* **2016,** *145* (1), 014504.

22. Fumagalli, L.; Hu, S.; Ares, P.; Janardanan, A.; Yang, Q.; Radha, B.; Novoselov, K. S.; Geim, A. K.; Esfandiar, A.; Fabregas, R.; Gomila, G.; Taniguchi, T.; Watanabe, K., Anomalously low dielectric constant of confined water. *Science* **2018,** *360* (6395), 1339-1342.
23. Benderskii, A.; Morita, A., Nonlinear spectroscopy and interfacial structure and dynamics. *J. Chem. Phys.* **2019,** *151* (15), 150401/1-150401/3.
24. Stiopkin, I. V.; Weeraman, C.; Pieniazek, P. A.; Shalhout, F. Y.; Skinner, J. L.; Benderskii, A. V., Hydrogen bonding at the water surface revealed by isotopic dilution spectroscopy. *Nature* **2011,** *474* (7350), 192-195.
25. Medders, G. R.; Paesani, F., Dissecting the Molecular Structure of the Air/Water Interface from Quantum Simulations of the Sum-Frequency Generation Spectrum. *J. Am. Chem. Soc.* **2016,** *138* (11), 3912-3919.
26. Ohno, P. E.; Wang, H.-f.; Paesani, F.; Skinner, J. L.; Geiger, F. M., Second-Order Vibrational Lineshapes from the Air/Water Interface. *J. Phys. Chem. A* **2018,** *122* (18), 4457-4464.
27. Reddy, S. K.; Thiraux, R.; Rudd, B. A. W.; Lin, L.; Adel, T.; Joutsuka, T.; Geiger, F. M.; Allen, H. C.; Morita, A.; Paesani, F., Bulk contributions modulate the sum-frequency generation spectra of water on model sea-spray aerosols. *Chem* **2018,** *4* (7), 1629-1644.
28. Poli, E.; Jong, K. H.; Hassanali, A., Charge transfer as a ubiquitous mechanism in determining the negative charge at hydrophobic interfaces. *Nat. Commun.* **2020,** *11* (1), 901.
29. Fan, Y.; Chen, X.; Yang, L.; Cremer, P. S.; Gao, Y. Q., On the Structure of Water at the Aqueous/Air Interface. *J. Phys. Chem. B* **2009,** *113* (34), 11672-11679.
30. Pezzotti, S.; Galimberti, D. R.; Shen, Y. R.; Gaigeot, M.-P., Structural definition of the BIL and DL: A new universal methodology to rationalize non-linear χ (2)(ω) SFG signals at charged interfaces, including χ (3)(ω) contributions. *Phys. Chem. Chem. Phys.* **2018,** *20* (7), 5190-5199.
31. Schmid, G. M.; Hurd, R. M.; Snavely, E. S., Jr., Effects of electrostatic fields on the surface tension of salt solutions. *J. Electrochem. Soc.* **1962,** *109*, 852-8.
32. Dang, L. X.; Chang, T.-M., Molecular dynamics study of water clusters, liquid, and liquid-vapor interface of water with many-body potentials. *J. Chem. Phys.* **1997,** *106* (19), 8149-8159.
33. Dang, L. X.; Chang, T.-M., Many-body interactions in liquid methanol and its liquid/vapor interface: A molecular dynamics study. *J. Chem. Phys.* **2003,** *119* (18), 9851-9857.
34. Kuo, I. F. W.; Mundy, C. J., An ab initio molecular dynamics study of the aqueous liquid-vapor interface. *Science* **2004,** *303* (5658), 658-660.
35. Chacon, E.; Tarazona, P.; Alejandre, J., The intrinsic structure of the water surface. *J. Chem. Phys.* **2006,** *125* (1), 014709/1-014709/10.
36. Kühne, T. D.; Pascal, T. A.; Kaxiras, E.; Jung, Y., New Insights into the Structure of the Vapor/Water Interface from Large-Scale First-Principles Simulations. *J. Phys. Chem. Lett.* **2011,** *2* (2), 105-113.
37. Tang, F.; Ohto, T.; Sun, S.; Rouxel, J. R.; Imoto, S.; Backus, E. H. G.; Mukamel, S.; Bonn, M.; Nagata, Y., Molecular Structure and Modeling of Water–Air and Ice–Air Interfaces Monitored by Sum-Frequency Generation. *Chem. Rev.* **2020,** *120* (8), 3633-3667.
38. Backus, E. H. G.; Schaefer, J.; Bonn, M., Probing the Mineral-Water Interface with Nonlinear Optical Spectroscopy. *Angew. Chem., Int. Ed.* **2021,** *60* (19), 10482-10501.
39. Hurd, R. M.; Schmid, G. M.; Snavely, E. S., Jr., Electrostatic fields, their effect on the surface tension of aqueous salt solutions. *Science* **1962,** *135*, 791-2.
40. Hayes, C. F., Water-air interface in the presence of an applied electric field. *J. Phys. Chem.* **1975,** *79* (16), 1689-93.
41. Jiang, Q.; Chiew, Y. C.; Valentini, J. E., Electric field effects on the surface tension of air/solution interfaces. *Colloids Surf. A* **1994,** *83* (2), 161-6.
42. Pethica, B. A., Electric Field Effects on Air/Solution Interfaces. *Langmuir* **1998,** *14* (11), 3115-3117.

43. Laanait, N.; Mihaylov, M.; Hou, B.; Yu, H.; Vanysek, P.; Meron, M.; Lin, B.; Benjamin, I.; Schlossman, M., Tuning ion correlations at an electrified soft interface. *Proc. Natl. Acad. Sci. U. S. A.* **2012,** *109* (50), 20326-20331, S20326/1-S20326/6.
44. Shen, Y. R., *The principles of Nonlinear Optics*. John Wiley: New York, 1984.
45. Zhao, X.; Ong, S.; Eisenthal, K. B., Polarization of water molecules at a charged interface. Second harmonic studies of charged monolayers at the air/water interface. *Chem. Phys. Lett.* **1993,** *202* (6), 513-20.
46. Corn, R. M.; Higgins, D. A., Optical second harmonic generation as a probe of surface chemistry. *Chem. Rev.* **1994,** *94* (1), 107-25.
47. Wang, H.; Borguet, E.; Eisenthal, K. B., Polarity of Liquid Interfaces by Second Harmonic Generation Spectroscopy. *J. Phys. Chem. A* **1997,** *101* (4), 713-718.
48. Boyd, R. W., *Nonlinear Optics*. Third Edition ed.; Academic Press, Inc.: 2008.
49. Ohno, P. E.; Wang, H.-f.; Geiger, F. M., Second-order spectral lineshapes from charged interfaces. *Nat. Commun.* **2017,** *8* (1), 1-9.
50. Dalstein, L.; Chiang, K.-Y.; Wen, Y.-C., Direct Quantification of Water Surface Charge by Phase-Sensitive Second Harmonic Spectroscopy. *J. Phys. Chem. Lett.* **2019,** *10* (17), 5200-5205.
51. Gonella, G.; Lütgebaucks, C.; de Beer, A. G. F.; Roke, S., Second Harmonic and Sum-Frequency Generation from Aqueous Interfaces Is Modulated by Interference. *J. Phys. Chem. C* **2016,** *120* (17), 9165-9173.
52. Wen, Y.-C.; Zha, S.; Liu, X.; Yang, S.; Guo, P.; Shi, G.; Fang, H.; Shen, Y. R.; Tian, C., Unveiling Microscopic Structures of Charged Water Interfaces by Surface-Specific Vibrational Spectroscopy. *Phys. Rev. lett* **2016,** *116* (1), 016101.
53. Urashima, S.-h.; Myalitsin, A.; Nihonyanagi, S.; Tahara, T., The Topmost Water Structure at a Charged Silica/Aqueous Interface Revealed by Heterodyne-Detected Vibrational Sum Frequency Generation Spectroscopy. *J. Phys. Chem. Lett.* **2018,** *9* (14), 4109-4114.
54. Pezzotti, S.; Galimberti, D. R.; Gaigeot, M.-P., 2D H-Bond Network as the Topmost Skin to the Air–Water Interface. *J. Phys. Chem. Lett.* **2017,** *8* (13), 3133-3141.
55. Shin, S.; Willard, A. P., Three-Body Hydrogen Bond Defects Contribute Significantly to the Dielectric Properties of the Liquid Water-Vapor Interface. *J. Phys. Chem. Lett.* **2018,** *9* (7), 1649-1654.
56. Joutsuka, T.; Morita, A., Electrolyte and Temperature Effects on Third-Order Susceptibility in Sum-Frequency Generation Spectroscopy of Aqueous Salt Solutions. *J. Phys. Chem. C* **2018,** *122* (21), 11407-11413.
57. Wang, H.-F., Sum frequency generation vibrational spectroscopy (SFG-VS) for complex molecular surfaces and interfaces: Spectral lineshape measurement and analysis plus some controversial issues. *Prog. Surf. Sci.* **2016,** *91* (4), 155-182.
58. Ohno, P. E.; Chang, H.; Spencer, A. P.; Liu, Y.; Boamah, M. D.; Wang, H.-f.; Geiger, F. M., Beyond the Gouy–Chapman Model with Heterodyne-Detected Second Harmonic Generation. *J. Phys. Chem. Lett.* **2019,** *10* (10), 2328-2334.
59. Mucha, M.; Frigato, T.; Levering, L. M.; Allen, H. C.; Tobias, D. J.; Dang, L. X.; Jungwirth, P., Unified Molecular Picture of the Surfaces of Aqueous Acid, Base, and Salt Solutions. *J. Phys. Chem. B* **2005,** *109* (16), 7617-7623.
60. Boamah, M. D.; Ohno, P. E.; Lozier, E.; Van Ardenne, J.; Geiger, F. M., Specifics about Specific Ion Adsorption from Heterodyne-Detected Second Harmonic Generation. *J. Phys. Chem. B* **2019,** *123* (27), 5848-5856.
61. Adel, T.; Ng, K. C.; Vazquez de Vasquez, M. G.; Velez-Alvarez, J.; Allen, H. C., Insight into the Ionizing Surface Potential Method and Aqueous Sodium Halide Surfaces. *Langmuir* **2021,** *37* (26), 7863-7874.
62. Sartin, M. M.; Sung, W.; Nihonyanagi, S.; Tahara, T., Molecular mechanism of charge inversion revealed by polar orientation of interfacial water molecules: A heterodyne-detected vibrational sum frequency generation study. *J. Chem. Phys.* **2018,** *149* (2), 024703.

63. Vargaftik, N. B.; Volkov, B. N.; Voljak, L. D., International tables of the surface tension of water. *J. Phys. Chem. Ref. Data* **1983,** *12* (3), 817-820.
64. Berry, J. D.; Neeson, M. J.; Dagastine, R. R.; Chan, D. Y. C.; Tabor, R. F., Measurement of surface and interfacial tension using pendant drop tensiometry. *J. Colloid Interface Sci.* **2015,** *454*, 226-237.
65. Reuther, A.; Laubereau, A.; Nikogosyan, D. N., Primary Photochemical Processes in Water. *J. Phys. Chem.* **1996,** *100* (42), 16794-16800.
66. Adams, E. M.; Verreault, D.; Jayarathne, T.; Cochran, R. E.; Stone, E. A.; Allen, H. C., Surface organization of a DPPC monolayer on concentrated SrCl2 and ZnCl2 solutions. *Phys. Chem. Chem. Phys.* **2016,** *18* (47), 32345-32357.
67. Adams, E. M.; Wellen, B. A.; Thiraux, R.; Reddy, S. K.; Vidalis, A. S.; Paesani, F.; Allen, H. C., Sodium-carboxylate contact ion pair formation induces stabilization of palmitic acid monolayers at high pH. *Phys Chem Chem Phys* **2017,** *19* (16), 10481-10490.
68. Lin, L.; Husek, J.; Biswas, S.; Baumler, S. M.; Adel, T.; Ng, K. C.; Baker, L. R.; Allen, H. C., Iron(III) Speciation Observed at Aqueous and Glycerol Surfaces: Vibrational Sum Frequency and X-ray. *J. Am. Chem. Soc.* **2019,** *141* (34), 13525-13535.
69. Zhuang, X.; Miranda, P. B.; Kim, D.; Shen, Y. R., Mapping molecular orientation and conformation at interfaces by surface nonlinear optics. *Phys. Rev. B: Condens. Matter Mater. Phys.* **1999,** *59* (19), 12632-12640.
70. Rao, Y.; Tao, Y.-s.; Wang, H.-f., Quantitative analysis of orientational order in the molecular monolayer by surface second harmonic generation. *J. Chem. Phys.* **2003,** *119* (10), 5226-5236.
71. Bian, H.-t.; Feng, R.-r.; Xu, Y.-y.; Guo, Y.; Wang, H.-f., Increased interfacial thickness of the NaF, NaCl and NaBr salt aqueous solutions probed with non-resonant surface second harmonic generation (SHG). *Phys. Chem. Chem. Phys.* **2008,** *10* (32), 4920-4931.
72. Ong, S.; Zhao, X.; Eisenthal, K. B., Polarization of water molecules at a charged interface: second harmonic studies of the silica/water interface. *Chem. Phys. Lett.* **1992,** *191* (3-4), 327-335.
73. Yan, E. C. Y.; Liu, Y.; Eisenthal, K. B., New method for determination of surface potential of microscopic particles by second harmonic generation. *J. Phys. Chem. B* **1998,** *102* (33), 6331-6336.
74. Salafsky, J. S.; Eisenthal, K. B., Protein adsorption at interfaces detected by second harmonic generation. *J. Phys. Chem. B* **2000,** *104* (32), 7752-7755.
75. Geiger, F. M., Second harmonic generation, sum frequency generation, and χ (3): dissecting environmental interfaces with a nonlinear optical Swiss Army knife. *Ann. Rev. Phys. Chem.* **2009,** *60*, 61-83.
76. Joutsuka, T.; Hirano, T.; Sprik, M.; Morita, A., Effects of third-order susceptibility in sum frequency generation spectra: a molecular dynamics study in liquid water. *Phys. Chem. Chem. Phys.* **2018,** *20* (5), 3040-3053.
77. Tian, C.; Ji, N.; Waychunas, G. A.; Shen, Y. R., Interfacial Structures of Acidic and Basic Aqueous Solutions. *J. Am. Chem. Soc.* **2008,** *130* (39), 13033-13039.
78. Hua, W.; Verreault, D.; Allen, H. C., Relative Order of Sulfuric Acid, Bisulfate, Hydronium, and Cations at the Air–Water Interface. *J. Am. Chem. Soc.* **2015,** *137* (43), 13920-13926.
79. Pezzotti, S.; Gaigeot, M.-P., Spectroscopic BIL-SFG Invariance Hides the Chaotropic Effect of Protons at the Air-Water Interface. *Atmosphere* **2018,** *9* (10), 396.
80. Sun, S.; Schaefer, J.; Backus, E. H. G.; Bonn, M., How surface-specific is 2nd-order non-linear spectroscopy? *J. Chem. Phys.* **2019,** *151* (23), 230901/1-230901/7.
81. Willard, A. P.; Chandler, D., Instantaneous Liquid Interfaces. *J. Phys. Chem. B* **2010,** *114* (5), 1954-1958.

For Table of Contents Only